Research Square

Preprints are preliminary reports that have not undergone peer review.
They should not be considered conclusive, used to inform clinical practice,
or referenced by the media as validated information.

Optimization of PGNAA Detector Shielding by Combining Monte Carlo Simulation with an Optimization Algorithm

Chenmin Xiao
Nanjing University of Aeronautics and Astronautics
Yumeng Cui
Nanjing University of Aeronautics and Astronautics
JiCheng Li
Nanjing University of Aeronautics and Astronautics
Yiying Li
Nanjing University of Aeronautics and Astronautics
ZiYang Gong
Nanjing University of Aeronautics and Astronautics
Jiajun Chen
Nanjing University of Aeronautics and Astronautics
Hongtao Wang
GRG Metrology & Test Group Co., Ltd
Can Cheng
Nanjing Tech University
Wenbao Jia
jiawb@nuaa.edu.cn

Nanjing University of Aeronautics and Astronautics

Research Article

Keywords: Prompt gamma neutron activation analysis, deuterium-tritium neutron generator, Geant4, detector shielding, signal-to-noise ratio

Posted Date: November 9th, 2026

DOI: https://doi.org/10.21203/rs.3.rs-11482424/v1

License: This work is licensed under a Creative Commons Attribution 4.0 International License.
Read Full License

Additional Declarations: No competing interests reported.

Optimization of PGNAA Detector Shielding by Combining Monte Carlo Simulation with an Optimization Algorithm

Chenmin Xiao[1], Yumeng Cui[1], JiCheng Li[1], Yiying Li[1], ZiYang Gong[1], Jiajun Chen[1], Hongtao Wang[3], Can Cheng[2], Wenbao Jia[1]

[1]Nanjing University of Aeronautics and Astronautics, 29 Jiangjun Avenue, Jiangning District, 211106 Nanjing, China

[2]Nanjing Tech University, 30 Puzhu South Road, Jiangbei New Area, 211816 Nanjing, China

[3]GRG Metrology & Test Group Co., Ltd., 511450 Guangzhou China

Abstract

Detector shielding is essential in prompt gamma neutron activation analysis (PGNAA) systems to attenuate neutrons reaching the detector and suppress gamma-ray background. A Monte Carlo simulation coupled with an optimization algorithm was used to optimize the detector shielding and detector-to-sample distance. Among 35 evaluated candidates, 8 cm Pb and 5 cm BPE at 33 cm yielded the highest simulated SNR of 0.209. Experiments with the same shield also gave the highest SNR of 0.157 at 33 cm, 185.5% higher than at 25 cm. The agreement between simulation and experiment demonstrates the effectiveness of the method.

Can Cheng chengcan@njtech.edu.cn
Wenbao Jia jiawenbao@163.com
1 Jiangning District, Nanjing University of Aeronautics And Astronautics, No. 29 Jiangjun Road, Nanjing 211106, Jiangsu Province, China
2 Pukou District, Nanjing Tech University, No. 30 Puzhu South Road, Nanjing 211899, Jiangsu Province, China

Keywords

Prompt gamma neutron activation analysis; deuterium-tritium neutron generator; Geant4; detector shielding; signal-to-noise ratio

1 Introduction

Elemental analysis is essential for determining the elemental composition and concentration of materials. X-ray fluorescence (XRF) is suitable for rapid multielement analysis of solids with minimal sample preparation. Inductively coupled plasma mass spectrometry (ICP-MS) provides excellent trace-element and isotopic analysis capabilities. Atomic absorption spectroscopy (AAS) is a mature method for element-selective quantification, whereas laser-induced breakdown spectroscopy (LIBS) enables rapid, in situ, and remote analysis [1–4]. However, these methods may be constrained by sample state, sampling representativeness, matrix effects, or sample-preparation requirements. By contrast, prompt gamma neutron activation analysis (PGNAA) identifies elements through characteristic prompt gamma rays emitted following neutron capture or inelastic scattering. PGNAA offers high penetration, requires little sample preparation, and supports the nondestructive analysis of large or enclosed objects [5]. It has therefore been applied in various fields, including the coal industry, environmental monitoring, metallurgy, and the nuclear energy sector [6–9].

The neutron-source type directly affects the configuration, radiation-field distribution, and engineering applicability of a PGNAA system. Reactor neutron sources provide high-flux, stable thermal-neutron beams suitable for high-precision offline analysis. However, their construction and shielding costs are high, limiting their use in industrial settings. Radioisotope neutron sources require no electrical power and have simple structures, but they cannot be switched off. They also impose substantial long-term safety-management and licensing burdens. D-D and D-T neutron generators offer electrical switching, adjustable output, compact structures, and straightforward integration [10, 11]. Recent studies have further demonstrated the development of high-yield D-D neutron generator-based PGNAA systems for quantitative elemental analysis, with shielding and collimation

optimization used to mitigate the increased radiation background associated with high neutron fluxes [27]. Their relatively high neutron yield from a compact source makes them suitable for industrial PGNAA systems designed for large samples. However, the moderation, scattering, and capture of high-energy fast neutrons produce complex secondary gamma radiation in shields, samples, and surrounding materials. The detector spectrum consequently contains multiple superimposed interference components.

Detector shielding is essential in PGNAA systems. High-density metals, such as lead and tungsten, are commonly used to attenuate gamma rays and scattered photons. Hydrogenous materials, such as polyethylene, moderate fast neutrons, whereas neutron absorbers, including borated polyethylene, boron carbide, and lithium-containing materials, reduce the thermal-neutron component near the detector. Previous studies have shown that shielding composition, layer arrangement, material thickness, and detector position can affect the spectral background and measurement performance of PGNAA systems [12–15]. Detector-shield design must therefore balance the target-peak response, continuum background, neutron-induced interference, and geometric detection efficiency. Because shielding parameters and detector distance can influence these quantities simultaneously, they should be evaluated as coupled design variables rather than adjusted independently.

Monte Carlo transport codes, such as MCNP and Geant4, can model the transport and energy deposition of neutrons, photons, electrons, and secondary particles. They are therefore widely used to design PGNAA shielding structures and predict detector responses [16, 21, 22]. However, the computational cost of point-by-point searches increases with the number of design variables and simulated particle histories. Manual trial-and-error searches may also explore coupled shielding and geometric variables inefficiently. Optimization algorithms can direct a limited evaluation budget towards promising regions of the parameter space [18–20]. Coupling such an algorithm with Monte Carlo transport therefore provides a practical strategy for searching coupled shielding and detector-distance parameters, while retaining physics-based evaluation of each candidate configuration.

In this study, detector shielding was optimized for a system comprising a D-T neutron generator and an HPGe detector. The optimization algorithm was coupled with Monte Carlo simulation. The simulation and experimental results showed that the optimized design improved the ROI SNR. These results validated the feasibility of the method and provide a basis for subsequent PGNAA system design.

2 PGNAA System and Benchmark Experiment

The experimental system comprised a D–T neutron generator, the moderator, a NaCl solution sample, the detector shield, a portable HPGe detector, and a multichannel spectrum-acquisition system. The D–T neutron generator, developed at East China University of Technology, produced 14.1 MeV neutrons. The moderator consisted of 10 cm of lead and 5 cm of polyethylene for neutron multiplication and moderation, respectively. The sample consisted of 2 L of a 100 g/L NaCl solution. The distance from the neutron source to the sample centre was 40 cm, and the distance from the sample centre to the detector front face was 25 cm. An ORTEC portable TRANS-SPEC-N system was used for gamma-ray detection. The overall experimental arrangement is shown in Figure 1.

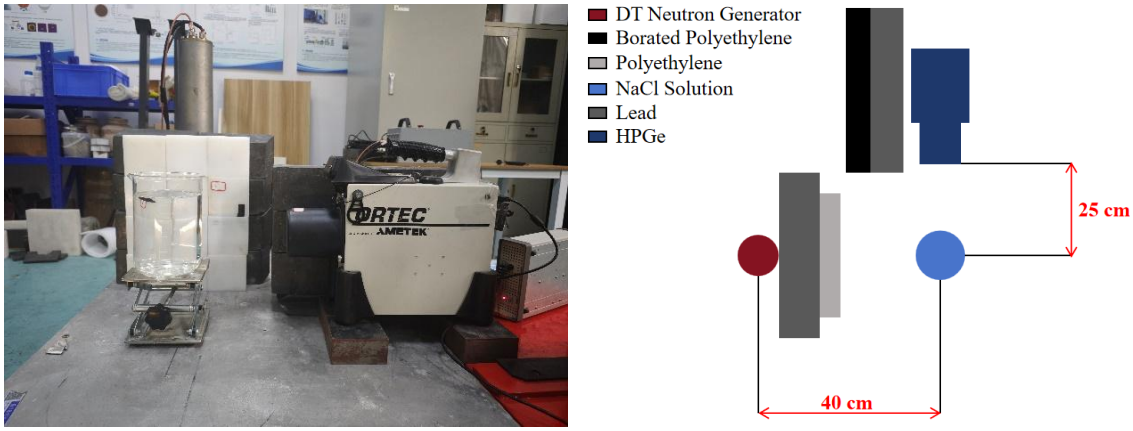


Fig. 1 Photograph (left) and schematic (right) of the D–T neutron generator-driven PGNAA experimental system

A benchmark experiment was first conducted using 8 cm of lead and 5 cm of borated polyethylene (BPE) as the detector shield. The detector front face was positioned 25 cm

from the sample centre. Spectra were acquired separately for the pure-water background and the NaCl solution sample, as shown in Figure 2.

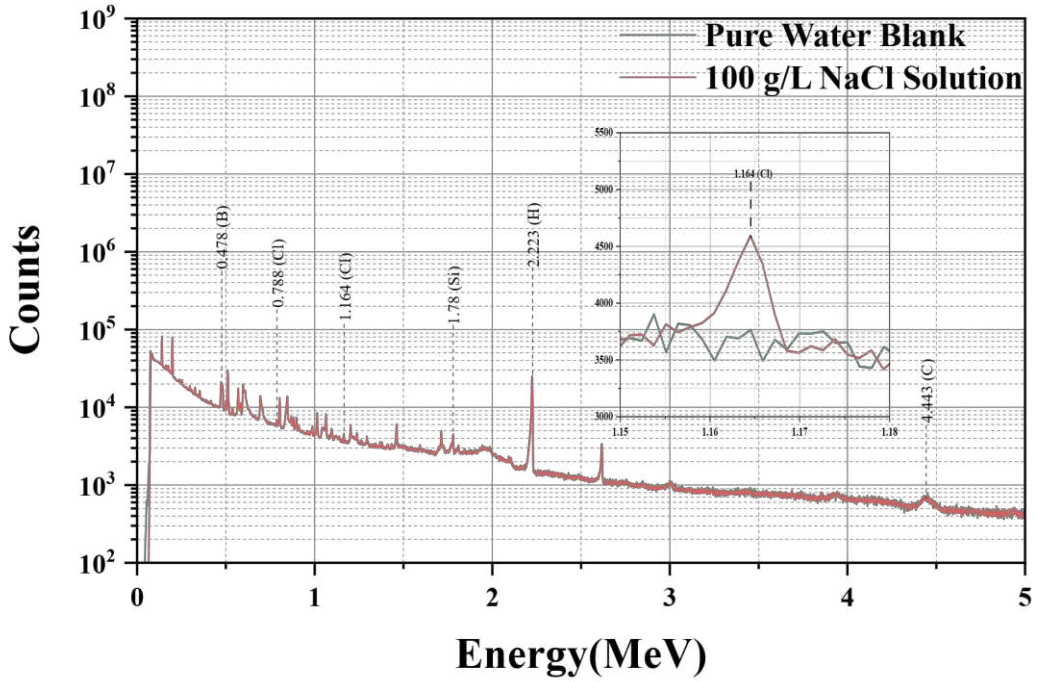


Fig. 2 Spectra measured in the benchmark experiment for the pure-water background and the NaCl solution sample

The 1.164 MeV prompt gamma-ray line of chlorine, produced by the 35Cl(n, γ)36Cl reaction, was selected as the target region of interest (ROI). According to Naqvi et al., the partial elemental gamma-ray production cross sections of the 1.164, 6.110, and 7.413 MeV chlorine lines are approximately 8.91, 6.59, and 3.29 barn, respectively [17]. The relatively large partial cross section of the 1.164 MeV line favours a strong prompt gamma-ray yield. Previous accelerator-based PGNAA measurements have also demonstrated the use of the approximately 1.165 MeV line for chlorine analysis [24]. For a given detector geometry, the full-energy peak efficiency of an HPGe detector generally decreases with increasing gamma-ray energy over the energy range considered here. At higher energies, incomplete energy deposition and the escape of annihilation photons following pair production can also produce single- and double-escape peaks [25]. Therefore, under the conditions of the present portable HPGe detector and D–T neutron generator-driven PGNAA system, the 1.164 MeV line provided a favourable combination of partial gamma-ray production cross

section, detection efficiency, and peak identifiability. Nevertheless, the measured energy region around 1.164 MeV contained a substantial Compton continuum and neutron-induced secondary gamma-ray background. The response of this region was therefore sensitive to changes in the detector shielding and measurement geometry.

Previous studies have shown that detector shielding and detector-to-sample distance can affect both the characteristic response and spectral background in PGNAA systems [12–15]. Following previous SNR-based evaluations of PGNAA system performance [15], the present study used an ROI-based metric to quantify changes in the sample and background responses. The energy interval surrounding the 1.164 MeV chlorine peak was used as the common ROI for all subsequent simulations and measurements.The ROI relative net-gain SNR was defined as

$$SNR = \frac{(C_{sample} - C_{bkg})}{C_{bkg}} \quad (1)$$

where C_{sample} and C_{bkg} denote the counts within the target Cl 1.164 MeV ROI in the sample and background spectra, respectively. All subsequent simulated candidate configurations and experimental distance responses used the same ROI and ROI relative net-gain SNR definition. This metric accounts for both the net target-peak increase and the background level.

The benchmark experiment was used to determine the energy-broadening parameters, target ROI interval, and relative weights of the direct gamma-response and neutron-induced energy-deposition channels. The same spectrum-response procedure and ROI definition were subsequently applied to all simulated candidate configurations and experimental measurements. This benchmark-constrained procedure provided a common basis for comparing different shielding and detector arrangements.

3 Monte Carlo Simulation and Optimization Algorithm

3.1 Geant4 Model

The Monte Carlo model was developed using Geant4 version 11.0.0. The model represented the experimental geometry, including the D–T neutron source, moderator, NaCl sample container, detector shield, and HPGe crystal [21, 22]. The QGSP_BIC_HP physics list was used to model neutron transport, neutron-capture reactions, and secondary gamma-ray production.

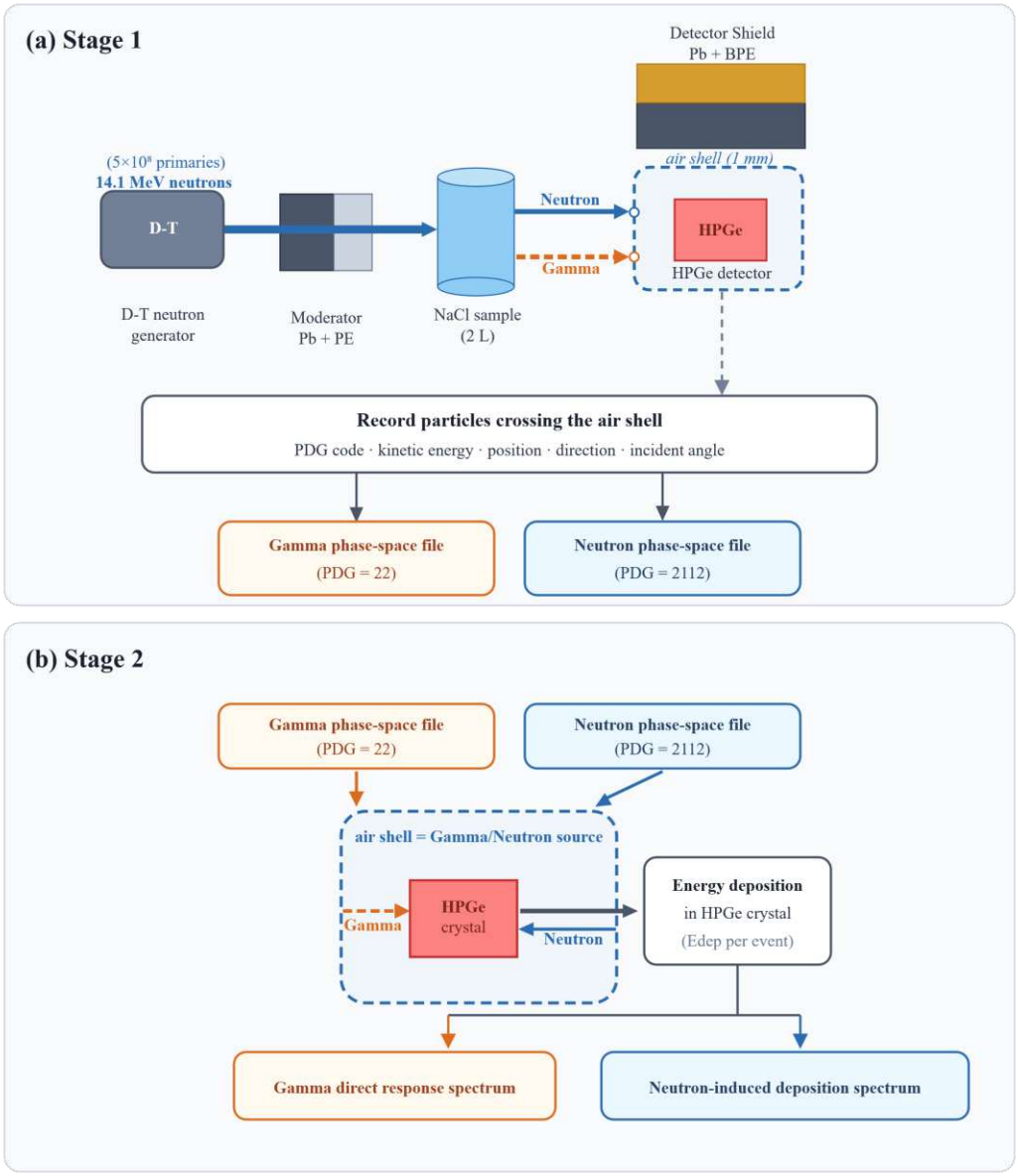


Fig. 3 Two-stage simulation procedure: (a) source transport and phase-space recording and (b) detector-response replay using the recorded photon and neutron phase-space files

The simulation workflow comprised source transport and detector-response replay, as shown in Figure 3. In the first stage, the D-T source emitted 5×10^8 neutrons at 14.1 MeV. A 1 mm-thick air layer enclosing the HPGe crystal served as the phase-space recording surface. When particles crossed this surface, the program recorded their Particle Data Group (PDG) codes, kinetic energies, direction vectors, spatial coordinates, and incidence angles. Gamma and neutron phase-space files were generated separately for PDG=22 and PDG=2112. In the second stage, both phase-space files were replayed separately as sources, and energy deposition in the HPGe crystal was recorded. Here, the term neutron-response spectrum denotes the total crystal energy-deposition spectrum produced after neutrons enter the detector vicinity. It includes scattering, capture, inelastic reactions, and associated secondary radiation, rather than the incident neutron kinetic-energy spectrum. Both response spectra underwent the same Gaussian energy broadening. They were then combined using fixed empirical weights constrained by the benchmark experiment for consistent evaluation of subsequent candidates. Energy broadening was calculated as follows:

$$FWHM = \sqrt{a + b \cdot E + c(E)^2} \tag{2}$$

where E and FWHM are expressed in MeV. Fitting the characteristic peaks at 0.511, 1.460, and 2.223 MeV yielded $a = 2.0837 \times 10^{-5}$ MeV^2, $b = -1.2291 \times 10^{-5}$ MeV, and $c = 8.5144 \times 10^{-6}$.The corresponding FWHM values were 0.00412, 0.00465, and 0.00593 MeV, respectively. These parameters were held constant for all candidate configurations to ensure consistent detector-response processing.

The benchmark spectrum was used to determine the relative weights of the direct gamma-response and neutron-induced energy-deposition channels. The two response components were adjusted by comparison with the hydrogen peak, the 1.164 MeV chlorine peak, and the continuum background in the benchmark spectrum. The selected neutron-to-gamma response-weight ratio was $f_n : f_\gamma = 100 : 180$, as shown in Figure 4. This empirical weighting was applied during spectral post-processing and did not modify the Geant4 particle-transport calculations. It was intended to reproduce the principal spectral features rather than provide a statistical fit to every local feature of the experimental spectrum. After

the weights had been determined, the same values were applied to all candidate configurations. No spectrum-specific adjustment was performed for different geometries.

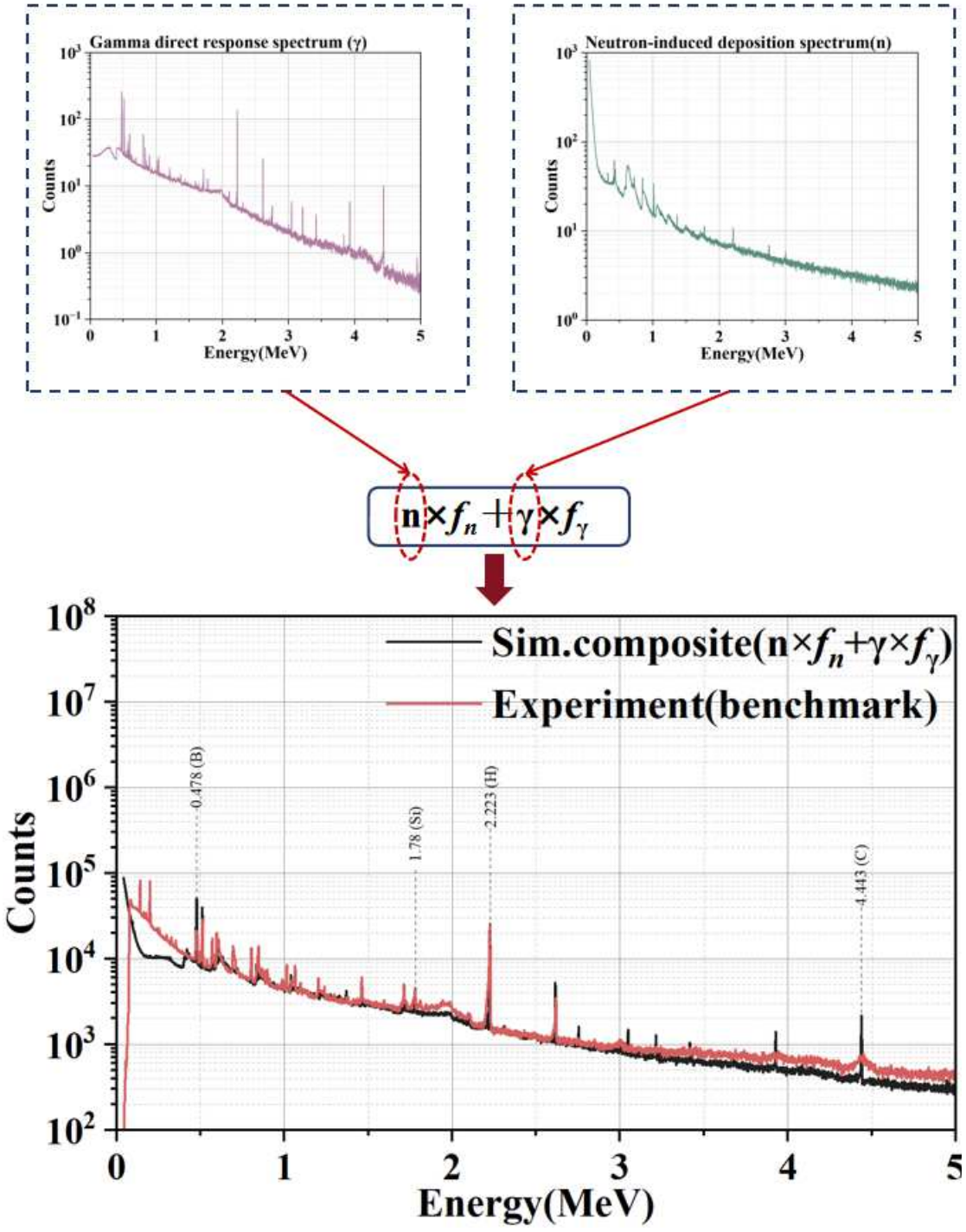


Fig. 4 Empirical weighting of the Geant4 direct gamma-response and neutron-induced energy-deposition spectra using the pure-water benchmark spectrum

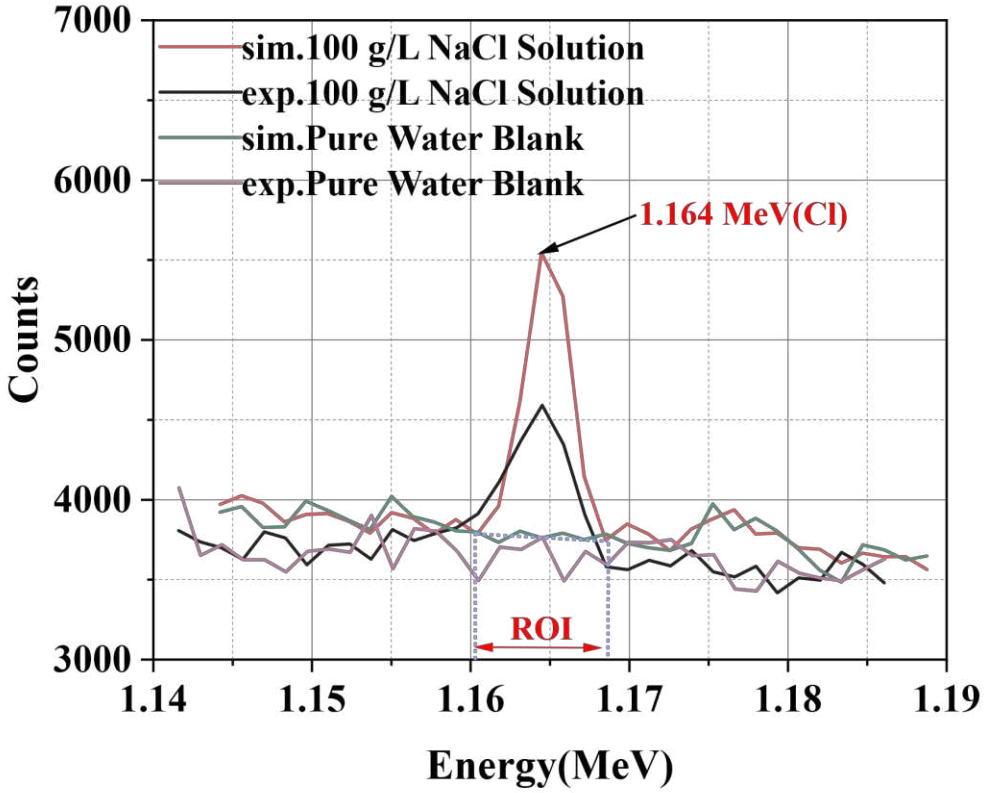


Fig. 5 Simulated and measured responses around the 1.164 MeV chlorine peak

Within the 1.164 MeV chlorine ROI shown in Figure 5, the continuum background contained two principal simulated components. The first was the Compton continuum produced by photons interacting in the HPGe crystal. The second arose from incomplete energy deposition by secondary photons generated in neutron-induced reactions.

The simulated and measured benchmark spectra showed the same target-peak position and similar overall background trends. This agreement was used to establish a common spectrum-response procedure for comparing candidate configurations. It did not indicate that the model reproduced every component of the experimental environment. The detector end cap, gaps in the shield assembly, laboratory scattering materials, source-output fluctuations, and electronic effects could influence the local peak shape and absolute counts. The model was therefore used primarily to compare relative responses among candidate configurations and identify regions with higher ROI relative net-gain SNRs.

Two transport cutoffs were applied during the first simulation stage to reduce the computational cost. The calculations were performed on an AMD Ryzen 9 5950X processor with 16 cores and 32 threads. First, G4UserStackingAction terminated newly generated electrons and positrons with kinetic energies below 0.4 MeV. The continuous-slowing-down approximation range of a 0.4 MeV electron in lead is approximately 0.23 mm [23], which is considerably smaller than the minimum Pb thickness of 3 cm. The influence of this cutoff on particles reaching the phase-space region was therefore expected to be small.

Second, G4UserSteppingAction recorded boundary-crossing events when particles entered the air shell. Photons with energies below 0.4 MeV were excluded from the phase-space files because an individual photon below this threshold cannot deposit energy within the 1.164 MeV target ROI. Together, these settings reduced the runtime of a single source-transport simulation from approximately 4.5 to 3 h.

3.2 Optimization Algorithm

Based on the benchmark-constrained spectrum-response procedure, the detector-shielding configuration and detector-to-sample distance were optimized using differential evolution (DE). The optimization variables were the BPE thickness, t_{BPE}, and the detector-to-sample distance, d. The Pb thickness, t_{Pb}, was derived from the fixed total shielding thickness: $t_{\mathrm{Pb}} + t_{\mathrm{BPE}} = 13$ cm. The BPE thickness was varied from 5 to 10 cm, corresponding to Pb thicknesses of 8 to 3 cm. The detector-to-sample distance was varied from 25 to 35 cm. The ROI relative net-gain SNR defined in Eq. (1) was used as the objective function.

Differential evolution (DE) is a population-based stochastic optimization algorithm based on mutation, crossover, and selection [18, 19]. In the present workflow, DE was used to generate candidate shielding configurations and detector-to-sample distances within the prescribed parameter space. Each candidate was evaluated using Geant4 phase-space replay and the fixed spectrum-response procedure described in Section 3.1.

The objective function was defined

$$f(\mathbf{x}) = -SNR(\mathbf{x}), \tag{3}$$

where $\mathbf{x} = (t_{\mathrm{BPE}}, d)$. Minimizing $f(\mathbf{x})$ was therefore equivalent to maximizing the background-normalized net increase within the 1.164 MeV chlorine ROI.

The optimization was implemented using the SciPy differential_evolution solver [26] and the best1bin strategy, corresponding to DE/best/1/bin. With a population-size multiplier of 6 and two optimization variables, the population contained 12 individuals. The maximum number of generations was 5. The mutation factor was varied from 0.5 to 1.0, and the crossover probability was set to 0.9. The random seed was 42, and the convergence tolerance was 0.001. The solver was allowed to terminate before reaching the maximum number of generations if its convergence criterion was satisfied.FCR

For individual i, the mutant vector was generated as

$$\boldsymbol{v}_i = \boldsymbol{x}_{best} + F(\boldsymbol{x}_{r1} - \boldsymbol{x}_{r2}) \tag{4}$$

where $\boldsymbol{x}_{best}$ is the best individual in the current population, and $\boldsymbol{x}_{r1}$ and $\boldsymbol{x}_{r2}$ are distinct randomly selected individuals. Crossover combined the mutant vector and original individual according to CR to generate a trial individual. If Geant4 evaluation gave the trial individual a higher SNR, it was retained in the next generation; otherwise, the original individual was retained. DE only scheduled candidate configurations. The SNR of each candidate was still calculated through Geant4 phase-space replay and benchmark-constrained spectrum-response modulation. Figure 6 shows the relationships among the benchmark constraint, gamma-neutron channel separation, Geant4 candidate evaluation, and DE search.

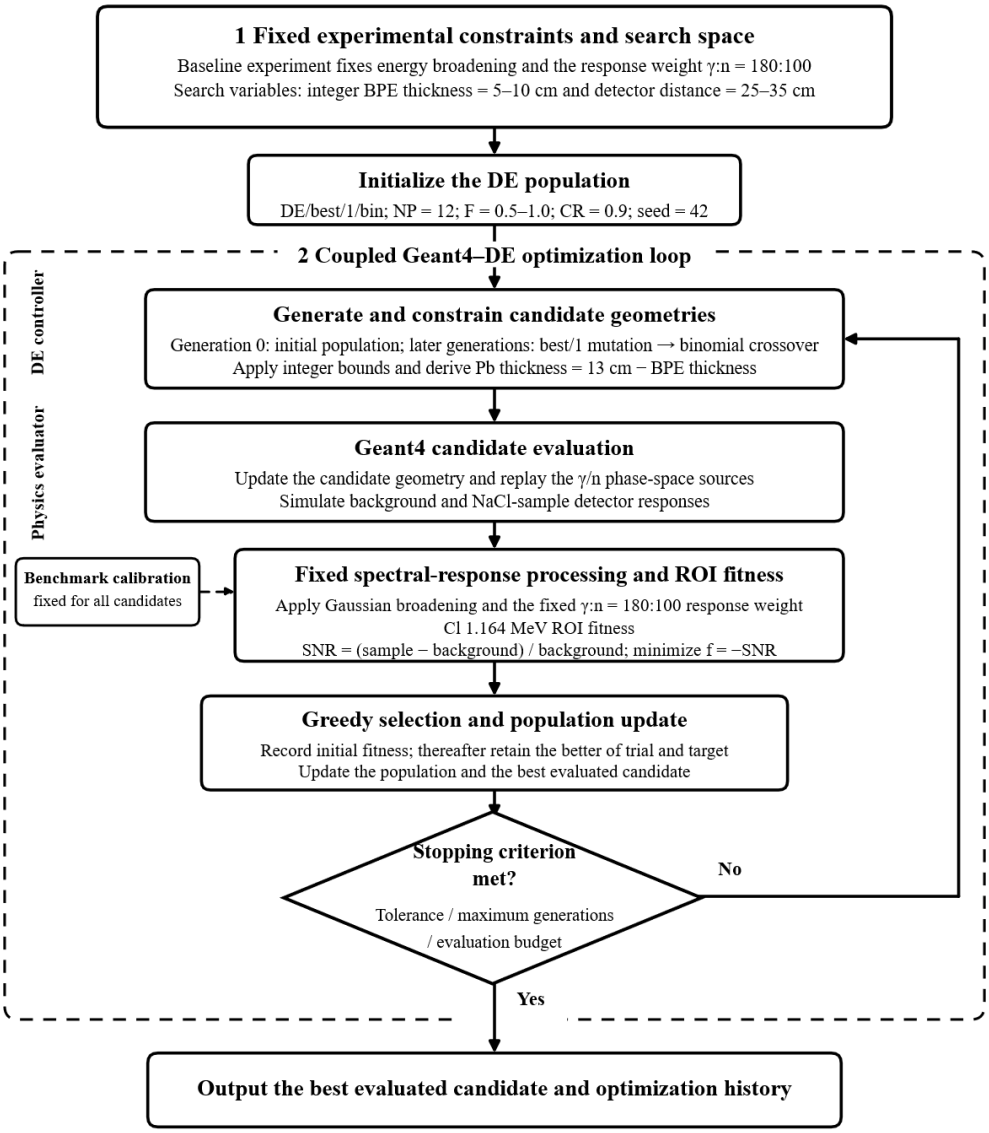


Fig. 6 Workflow linking benchmark calibration, Geant4 candidate evaluation, fixed spectrum-response processing, and DE-based candidate selection

4 Results and Discussion

4.1 Optimization Results

Using the fixed energy-broadening parameters and a neutron-to-gamma response-weight ratio of 100:180, DE proposed candidate configurations according to the search parameters and selection procedure described in Section 3.2. A total of 35 candidate

configurations were evaluated. Figures 7–9 show the distribution of population SNRs across generations, the evaluated configurations in the parameter space, and the evolution of the cumulative best SNR, respectively. These figures describe the search conducted in this study and do not provide a performance comparison with a complete grid search.

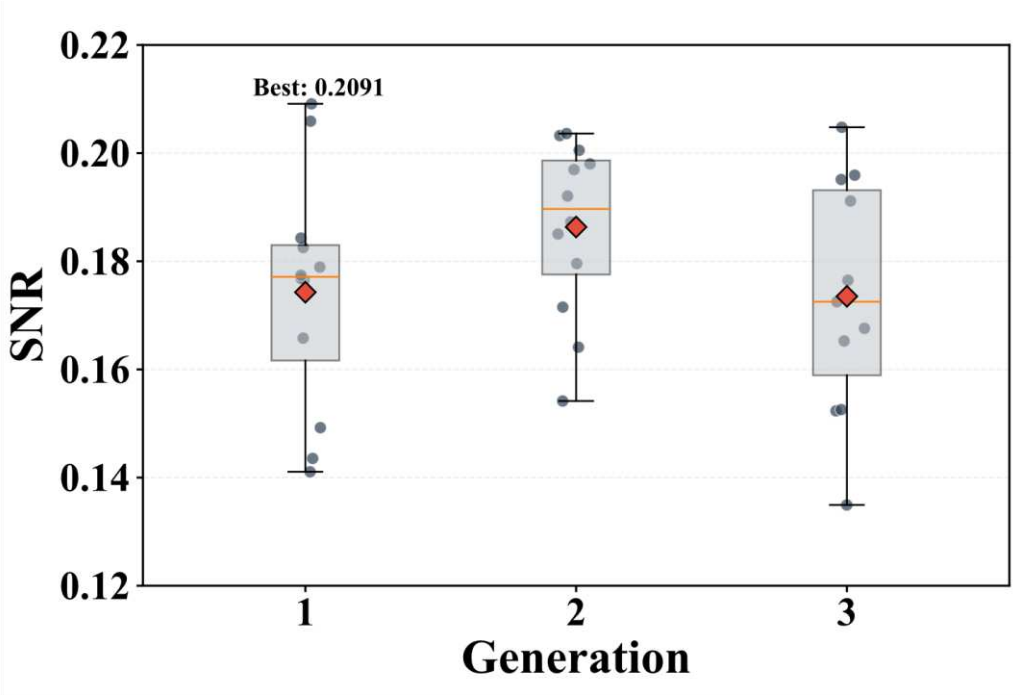


Fig. 7 Distribution of population SNRs across generations during DE optimization

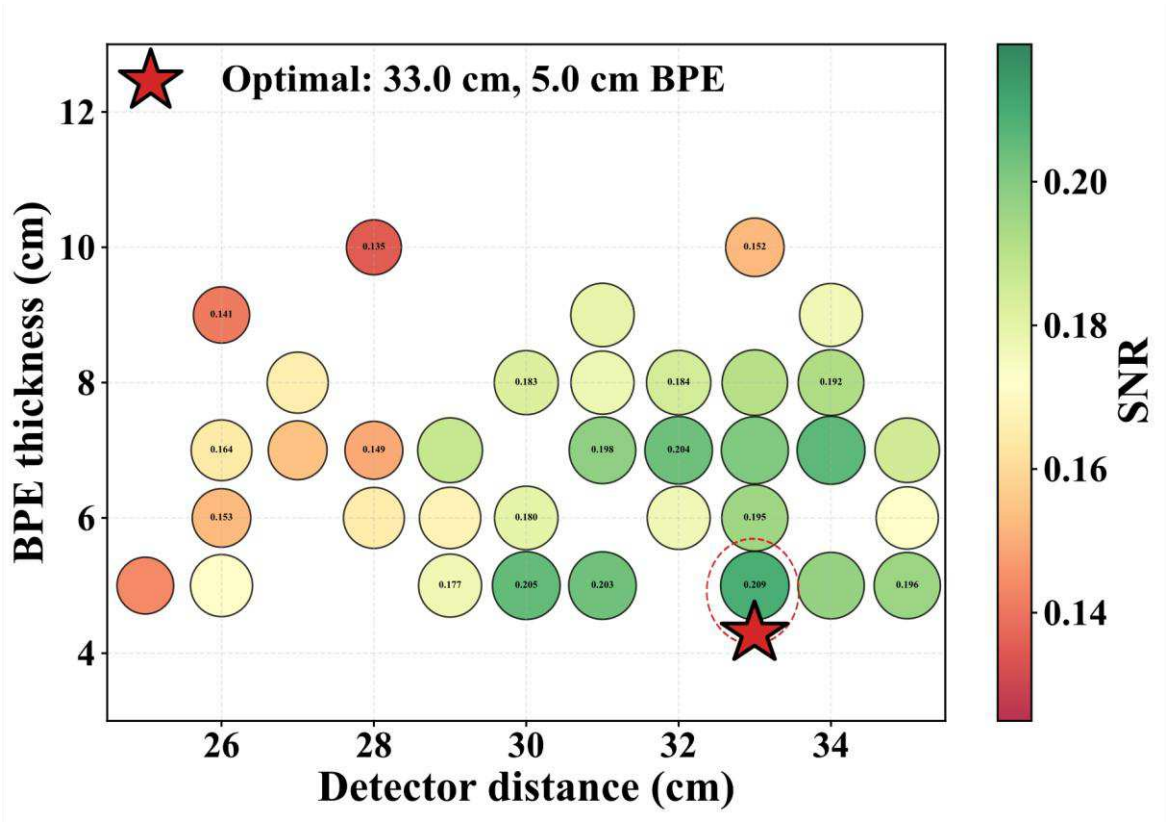


Fig. 8 Candidate configurations evaluated in the BPE-thickness and detector-to-sample distance parameter space

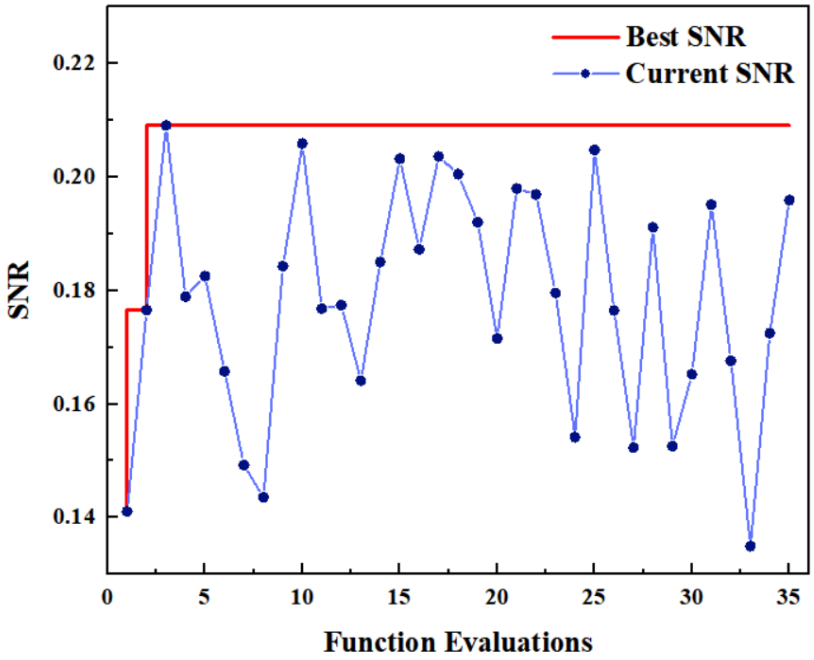


Fig. 9 Evolution of the candidate SNR and cumulative best SNR during DE optimization

As shown in Figure 7, candidates with higher SNRs became more frequent in the later generations. This pattern reflects the progressive concentration of the DE search in regions associated with higher objective values. Figure 8 shows the distribution of the 35 evaluated configurations in the BPE-thickness and detector-to-sample distance parameter space. Higher-SNR configurations were observed mainly at BPE thicknesses of 5–8 cm and detector-to-sample distances of 30–35 cm.

Figure 9 shows the SNR obtained for each evaluated configuration and the corresponding cumulative best value. The SNRs of the first three configurations were 0.135, 0.179, and 0.209, respectively. The cumulative best SNR reached 0.2091 after the third evaluation and remained unchanged during the subsequent evaluations. The remaining evaluations sampled additional regions of the prescribed parameter space but did not produce a higher SNR.

The evaluated SNRs did not vary monotonically with either the Pb/BPE thickness ratio or the detector-to-sample distance. Configurations with the same distance or similar shielding thicknesses could produce different SNRs. The response therefore depended on the combined selection of the shielding composition and detector position. Within the evaluated configurations, increasing an individual material thickness or the detector-to-sample distance did not consistently improve the SNR. Because only 35 configurations were evaluated, the observed distribution represents the sampled response rather than a complete response surface over the entire parameter space.

Among the evaluated candidates, the highest simulated SNR was obtained using 8 cm of Pb and 5 cm of BPE at a detector-to-sample distance of 33 cm. The simulated background and sample ROI counts were 15,828 and 19,138, respectively, corresponding to 3,310 net counts and an ROI relative net-gain SNR of 0.209. This response is consistent with the combined effects of gamma-ray attenuation by Pb, neutron moderation and absorption by BPE, and the distance-dependent changes in both the target response and mixed-field background. The identified configuration is specific to the apparatus, parameter space, and evaluation procedure used in this study.

Table 1 Simulated ROI responses for the benchmark configuration and the highest-SNR evaluated configuration

Evaluation case	Pb/BPE configuration	Detector-to-sample distance (cm)	Background ROI counts	Net counts	SNR
Best simulated point	8 cm Pb + 5 cm BPE	33	15828	3310	0.209
Simulated benchmark point	8 cm Pb + 5 cm BPE	25	33850	4859	0.144

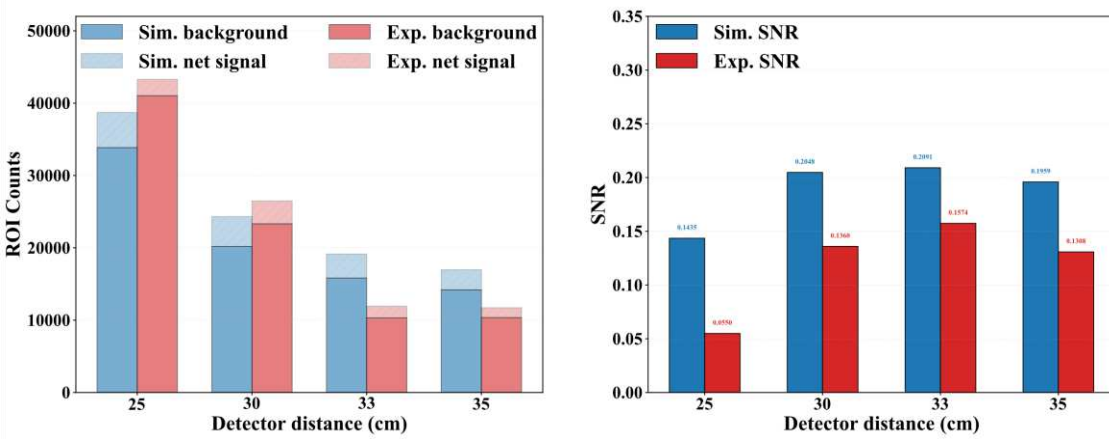
Based on these results, the 8 cm Pb + 5 cm BPE configuration at 33 cm was selected for experimental testing. Additional measurements at 30 and 35 cm, together with a benchmark point, were used as validation experiments intended to improve simulation accuracy. The experiment examined whether the best detection distance identified by simulation was consistent with the measured trend. It thereby evaluated the methodological feasibility of the workflow under the present system conditions.

4.2 Experimental Validation

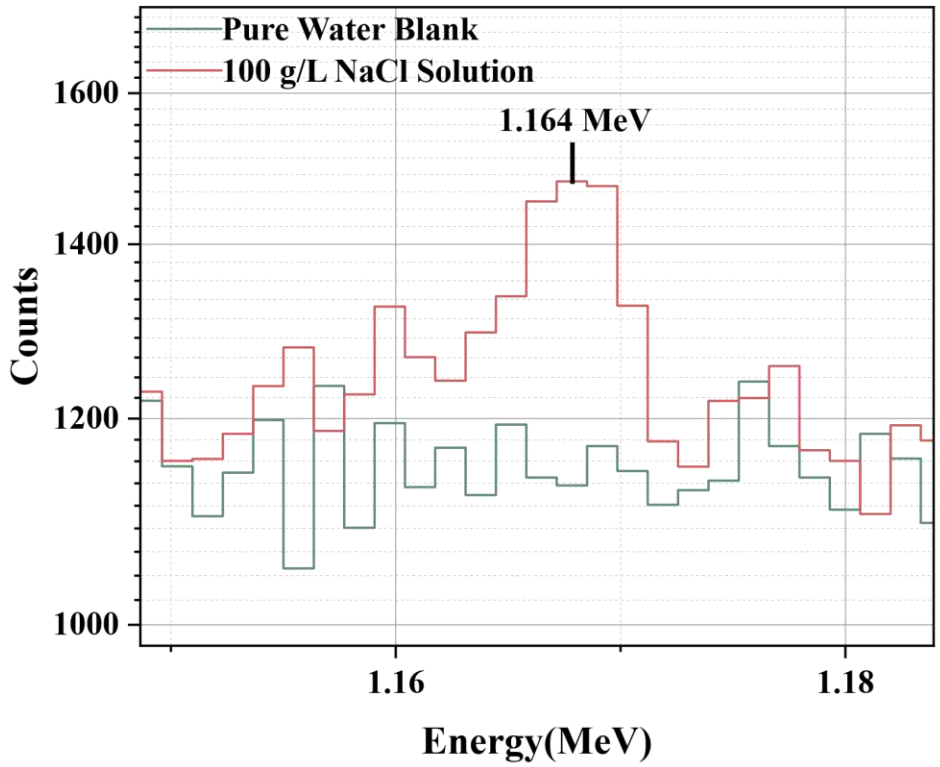
Experimental measurements were conducted using the 8 cm Pb + 5 cm BPE shield at detector-to-sample distances of 25, 30, 33, and 35 cm. The same NaCl solution sample, source-to-sample distance, moderator configuration, spectrum-acquisition procedure, and ROI calculation method were used at each distance. The resulting experimental SNRs are listed together with the simulated values in Table 2. Among the four measured distances, the highest experimental SNR was 0.157 at 33 cm. This value was 185.5% higher than the SNR of 0.055 measured at 25 cm.

Table 2 Simulated and experimental distance-response SNRs for the 8 cm Pb + 5 cm BPE configuration

Distance/cm	Simulated SNR	Experimental SNR
25	0.144	0.055
30	0.205	0.136
33	0.209	0.157
35	0.196	0.131



314 **Fig. 10** Simulated and experimental responses at four detector-to-sample distances for the
315 8 cm Pb + 5 cm BPE configuration: (a) ROI counts and (b) ROI relative net-gain SNR



316

317 **Fig. 11** Measured pure-water background and NaCl solution spectra for the 8 cm Pb + 5
318 cm BPE configuration at a detector-to-sample distance of 33 cm

319 As shown in Figure 10, the simulated SNRs at 25, 30, 33, and 35 cm were 0.144,
320 0.205, 0.209, and 0.196, respectively. The corresponding experimental values were 0.055,

0.136, 0.157, and 0.131. The simulated and experimental results followed the same ordering across the four distances, with the highest SNR occurring at 33 cm in both cases.

The simulated SNRs were consistently higher than the experimental values. The comparison therefore supports qualitative agreement in the distance-response pattern but does not establish numerical agreement or absolute model accuracy. Figure 11 shows the measured background and NaCl solution spectra obtained at 33 cm. A distinct response was observed near the 1.164 MeV chlorine peak in the sample spectrum.

Both the simulated and experimental SNRs increased from 25 to 33 cm and decreased at 35 cm. Changes in the detector-to-sample distance affected both the sample and background ROI counts, and the relative changes in these quantities determined the ROI relative net-gain SNR. The agreement in the location of the highest response supports the simulated distance-response prediction for the selected shielding configuration. However, this comparison was limited to four distances and did not independently validate the relative performance of different Pb/BPE shielding configurations.

5 Conclusions

This study established a PGNAA detector-shielding design workflow integrating benchmark-constrained Geant4 spectrum-response modulation, phase-space recording and replay, and differential evolution optimization. The benchmark spectrum fixed the empirical weights of the direct gamma-response and neutron-induced energy-deposition channels, and candidate configurations were evaluated using a common ROI relative net-gain SNR. Among the evaluated candidates, the best-performing configuration was 8 cm Pb plus 5 cm BPE at a detection distance of 33 cm. The simulated SNR was 0.209, while the highest experimental SNR was 0.157 at 33 cm, 185.5% above that at 25 cm. The agreement provided a preliminary consistency check for distance selection under the present system conditions. Future work can incorporate additional design variables, multiple ROIs, multi-objective optimization, and repeated measurements to evaluate result stability.

Within the investigated parameter space and optimization workflow, the best-performing configuration among the evaluated candidates was 8 cm Pb plus 5 cm BPE at a detection distance of 33 cm. The simulated background ROI, sample ROI, and net counts were 15,828, 19,138, and 3,310, respectively, giving a simulated SNR of 0.209. Experiments compared distances of 25, 30, 33, and 35 cm. The highest experimental SNR was 0.157 at 33 cm, representing a 185.5% increase over that at 25 cm. Simulation and experiment identified the same best detection distance among the four compared points. This agreement provided a preliminary consistency check for distance selection under the present system conditions. Future work can incorporate additional design variables, multiple ROIs, and multi-objective optimization. Repeated measurements can also be used to evaluate result stability.

Acknowledgements

This work was funded by National Natural Science Foundation of China (12575322) and National Science and Technology Major Project (2026ZD1612100).

References

1. Beckhoff B, Kanngießer B, Langhoff N et al (2006) Handbook of Practical X-Ray Fluorescence Analysis. Springer, Berlin.

2. Houk RS, Fassel VA, Flesch GD et al (1980) Inductively coupled argon plasma as an ion source for mass spectrometric determination of trace elements. Anal Chem 52:2283–2289. https://doi.org/10.1021/ac50064a012

3. Walsh A (1955) The application of atomic absorption spectra to chemical analysis. Spectrochim Acta 7:108–117. https://doi.org/10.1016/S0371-1951(00)80013-6

4. Miziolek AW, Palleschi V, Schechter I (2006) Laser-Induced Breakdown Spectroscopy: Fundamentals and Applications. Cambridge University Press, Cambridge.

5. Abdelnour MR, Liu J, Hossny K et al (2025) Prompt gamma neutron activation analysis: A review of applications, design, analytics, challenges, and prospects. Radiat Phys Chem 234:112693. https://doi.org/10.1016/j.radphyschem.2025.112693

6. Roy T, Shukla S, Kashyap Y et al (2024) Determination of moisture content in coal using pulsed fast thermal neutron activation technique. Radiat Phys Chem 222:111830.

7. Naqvi AA, Maslehuddin M, Kalakada Z et al (2014) Prompt gamma ray evaluation for chlorine analysis in blended cement concrete. Appl Radiat Isot 94:8–13.

8. Idiri Z, Mazrou H, Amokrane A et al (2010) Characterization of an Am–Be PGNAA set-up developed for in situ liquid analysis: Application to domestic waste water and industrial liquid effluents analysis. Nucl Instrum Methods Phys Res B 268:213–218.

9. Zhao L, Xu X, Lu JB et al (2021) Optimization of PGNAA device and algorithm for testing basicity index of sinter mixture. Nucl Sci Tech 32:6.

10. Chen SY, Li GH, Jia SL et al (2022) Design and optimization of a PGNAA system based on D-D neutron generator for cement composition analysis. Proc ICONE29 V015T16A067. https://doi.org/10.1115/ICONE29-91972

11. Cheng C, Wei ZY, Hei DQ et al (2019) Design of a PGNAA facility using D-T neutron generator for bulk samples analysis. Nucl Instrum Methods Phys Res B 452:30–35. https://doi.org/10.1016/j.nimb.2019.05.021

12. Ghasemi Z, Hassanvand M, Choopan Dastjerdi MH, Mokhtari J (2023) Design of a radiation shield for an HPGe detector for a reactor-based PGNAA facility. Radiat Phys Chem 210:111045. https://doi.org/10.1016/j.radphyschem.2023.111045

13. Jafari M, Jafari H, Choopan Dastjerdi MH, Mokhtari J (2024) Improvement of detector shield in PGNAA facility for boron concentration measurement. Heliyon 10:e39318. https://doi.org/10.1016/j.heliyon.2024.e39318

14. Jia WB, Hei DQ, Cheng C et al (2014) Optimization of PGNAA set-up for the elements detection in aqueous solution. Sci China Technol Sci 57:625–629. https://doi.org/10.1007/s11431-014-5469-5

15. Li JT, Jia WB, Hei DQ et al (2022) Research on the optimization method for PGNAA system design based on signal-to-noise ratio evaluation. Nucl Eng Technol 54:2221–2229. https://doi.org/10.1016/j.net.2021.12.034

16. Cardoso HAC, Melo SB, Meric I (2025) Modeling and geometrization in PGNAA. Comput Phys Commun 306:109360. https://doi.org/10.1016/j.cpc.2024.109360

17. Naqvi AA, Kalakada Z, Al-Anezi MS et al (2014) Performance evaluation of a portable neutron generator for prompt gamma-ray applications. Arab J Sci Eng 39:531–539. https://doi.org/10.1007/s13369-013-0880-y

18. Storn R, Price K (1997) Differential evolution: A simple and efficient heuristic for global optimization over continuous spaces. J Glob Optim 11:341–359. https://doi.org/10.1023/A:1008202821328

19. Das S, Suganthan PN (2011) Differential evolution: A survey of the state-of-the-art. IEEE Trans Evol Comput 15:4–31. https://doi.org/10.1109/TEVC.2010.2059031

20. Prozorova IV (2022) Integration of the differential evolution algorithm and the Monte Carlo code to create a spectrometric detector model. J Phys Conf Ser 2155:012020. https://doi.org/10.1088/1742-6596/2155/1/012020

21. Agostinelli S, Allison J, Amako K et al (2003) Geant4: A simulation toolkit. Nucl Instrum Methods Phys Res A 506:250–303. https://doi.org/10.1016/S0168-9002(03)01368-8

22. Allison J, Amako K, Apostolakis J et al (2006) Geant4 developments and applications. IEEE Trans Nucl Sci 53(1):270–278. https://doi.org/10.1109/TNS.2006.869826

23. Berger MJ, Coursey JS, Zucker MA, Chang J (2005) ESTAR, PSTAR, and ASTAR: Computer Programs for Calculating Stopping-Power and Range Tables for Electrons, Protons, and Helium Ions (version 1.2.3). National Institute of Standards and Technology, Gaithersburg, MD. https://physics.nist.gov/Star. Accessed 22 October 2026.

24. Naqvi AA, Nagadi MM, Al-Amoudi OSB (2006) Interferences in prompt gamma analysis of corrosive contaminants in concrete. Nucl Instrum Methods Phys Res A 569:803–809. https://doi.org/10.1016/j.nima.2006.09.058

25. Knoll GF (2010) Radiation Detection and Measurement, 4th edn. Wiley, Hoboken, NJ.

26. Virtanen P, Gommers R, Oliphant TE et al (2020) SciPy 1.0: Fundamental algorithms for scientific computing in Python. Nat Methods 17:261–272. https://doi.org/10.1038/s41592-019-0686-2

27. Li J, He X, Chen W, Wang Z, Xiao C, Cheng C, Jia W, Song J, Zou J, Shan Q (2026) Development of PGNAA setup for elemental analysis based on high-yield DD neutron generator. Nucl Eng Technol 58(7):104282. https://doi.org/10.1016/j.net.2026.104282